Optical Detection of Deeply Subwavelength Nanoparticles for Silicon Metrology

Anton Sofronov,* Boris Afinogenov, Anton Medvedev, Aleksandr Shorokhov, Maksim Riabko, and Stanislav Polonsky

Samsung R&D Institute Russia, Moscow 127018, Russia

(Received 29 March 2021; revised 19 May 2021; accepted 27 May 2021; published 21 June 2021)

We report on experimental detection of 10 nm Si nanoparticles on Si surface using spatial modulation microscopy. We show that a simple optical layout with a galvo-mirror allows reliable detection of 9×10 nm Si nanocylinders with signal-to-noise ratio 4.6 when the wavelength is tuned to the spectral range of direct-band optical transitions in silicon. We also show the possibility to use the spatial modulation microscopy principles for nonabsorbing particles. We demonstrate successful detection of Si nanocylinders down to 20×40 nm by scattered light ($\lambda = 680$ nm) analysis. Our results pave the way to an inspection method for semiconductor metrology.

DOI: 10.1103/PhysRevApplied.15.064049

I. INTRODUCTION

Nowadays, the semiconductor industry is one of the most rapidly developing areas. It implements the most recent research results and cutting-edge technologies with rigorous demands on the manufacturing process and quality control, including semiconductor metrology. Together with advanced methods of device metrology at different production stages [1], inspection of unpatterned wafers now, as in the past, is a necessary part of the production process [2]. Particles, including Si particles, generated within the process equipment during mechanical and wafer processing operations and adhered to the wafer surface can cause defects responsible for a considerable part of yield loss.

The current technology nodes in the semiconductor industry impose stiff requirements on particle sizes because even sub-10-nm particles can cause "killer defects." Change of a mainstream logic device architecture from finFET to lateral gate-all-around coming in 2025 further shrinks a critical particle size to 6 nm according to the recent International Roadmap for Devices and Systems (IRDS) [3]. Widely used industrial light-scattering-based wafer scanners can hardly detect such deeply subwavelength particles. Recent advances in optical design of scattering-based approaches allow the detection of 20 nm silicon nanoparticles on bare polished Si wafers [4]. Further improvement in minimum detection size is limited by the V^2 scaling of the scattering cross-section σ_s of the nanoparticle with its volume V.

A number of lab-level methods of single nanoparticle detection, including photothermal heterodyne imaging [5], four-wave mixing microscopy [6,7], and interferometric cross-polarization microscopy [8,9], demonstrate the detection of even 5-nm metallic nanoparticles experimentally. However, most of them exploit a strong plasmon resonance of metallic nanoparticles and are unlikely to give measurable signals from silicon nanoparticles. A number of technical limitations, such as immersion objective lenses, prevent its use in industrial wafer-level silicon metrology. Thus, the development of advanced methods for Si nanoparticle detection with sub-10-nm detectivity threshold applicable for the whole 300-mm wafer inspection within reasonable measurement time is of great importance.

Recently, we implemented nonlinear photoluminescence (PL) [10] and second harmonic generation (SHG) [11] microscopy of ultrafine defects (nanohills) on a silicon surface. The physical origin of contrast in PL microscopy is related to weak enhancement of electric field of both pump and PL. In the case of SHG microscopy the contrast is believed to rise due to symmetry restrictions of surface SHG at certain configurations that should be relaxed by surface defects. However, the limiting factors for both methods were found to be (i) low overall optical response of silicon due to its indirect band structure leading to a large radiative recombination time and low surface/bulk nonlinear susceptibility, and (ii) extremely low contrast of the signal from the subwavelength silicon surface defects against the background signal from surrounding surface.

A good recipe for elimination of the background is a differential measurement technique. Spatial modulation

*a.sofronov@samsung.com

microscopy (SMM) realizes this simple idea with periodical nanoparticle movement in and out of a laser beam waist with corresponding small intensity change measurement by a lock-in technique [12]. This principle allows the measurements of absorption cross-section of a single metallic nanoparticle down to 5 nm in diameter in transmission mode with different experimental setup implementations [13–15], along with the large extinction cross-section of carbon microparticles [16]. Owing to its high sensitivity and potentially high throughput, SMM is a promising candidate to enhance the performance of traditional optical inspection tools, serving as an extension of laser scanning microscopy.

However, up to now, there has been no research of SMM applications to the detection of technologically important nanoparticles, including silicon nanoparticles. In addition, owing to its absorption-based nature, the possibility of the detection of nonabsorbing scattering nanoparticles such as polystyrene spheres used for calibration of industrial wafer scanners [2] is unclear.

In this work, we report on experimental detection of single 10-nm silicon nanocylinders on silicon surface with an absorption-based SMM. We also show how the SMM principles can be applied to the nonabsorbing nanoparticles. We show, that SMM principles are potentially suitable for industry-level silicon metrology and can be applied to the far-field optical inspection of 300-mm pristine wafers with reasonable throughput.

II. SPATIAL MODULATION MICROSCOPY OF SUBWAVELENGTH ABSORBERS AND SCATTERERS

The main idea of SMM is to scan the sample with simultaneous fast oscillation of the laser spot position at the surface with the amplitude of the order of the spot size. The reflected light power is then measured with photodiode and lock-in amplifier at the oscillation frequency at every scan step. This allows one to measure only the difference signal between the neighbor areas of the sample surface with high signal-to-noise ratio (SNR) due to lock-in detection. When the nanoparticle moves across the spot, it changes the reflected intensity due to absorption or scattering of light.

In this section, we consider a small particle located at point (x_p, y_p) on the surface of generally opaque medium with reflection coefficient R [Fig. 1(a)]. The surface is illuminated with a tightly focused Gaussian laser beam with the total power P_i centered at (x_c, y_c), the intensity distribution in the beam waist of width ω_0 is

$$I(x,y) = \frac{2P_i}{\pi\omega_0^2}\exp\left(-2\frac{(x-x_c)^2+(y-y_c)^2}{\omega_0^2}\right). \quad (1)$$

In a simple case when the particle's absorption dominates over scattering [12–15], the reflected beam power P_r modified by the presence of the particle is

$$P_r = P_0 - \sigma_a I(x_p, y_p), \quad (2)$$

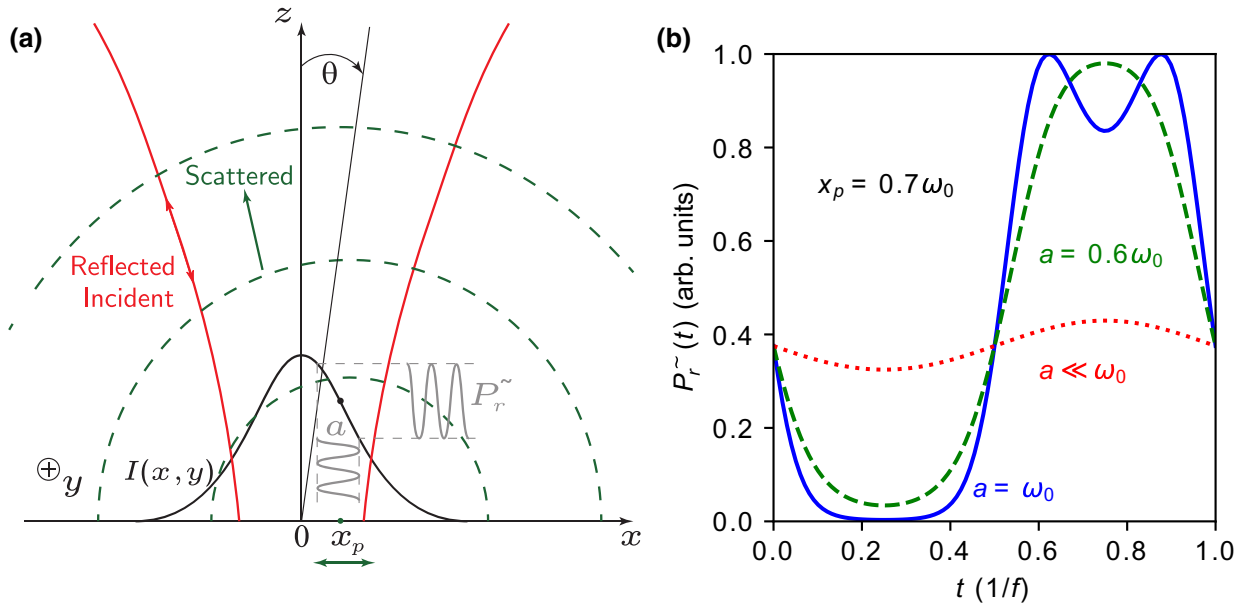

FIG. 1. (a) Schematics of the deeply subwavelength particle under the focused laser beam. Red lines show the incident (and reflected) beam profile, the black line shows the distribution of intensity in the focal plane. The particle at x_p absorbs or scatters incident light, corresponding scattered spherical wavefronts are shown with green dashed lines. Periodical movement of the particle leads to small periodic variation of the reflected power and/or the part of the total power result from the interference between scattered and reflected light. (b) One period of time-dependent part of the reflected beam power at different spatial modulation amplitudes (lock-in input).

where $P_0 = RP_i$ is the power of the beam reflected from the clean surface and σ_a is the particle absorption cross-section.

In order to detect such a small variation in reflected signal one can periodically change the position of the spot center with respect to the particle (or visa versa), so the difference $(x_p - x_c) = a\sin(2\pi ft)$ changes in time with frequency f and amplitude a. This leads to modulation of the power of the reflected beam

$$P_r(t) = P_0 - \sigma_a I(x_p + a\sin(2\pi ft), y_p), \tag{3}$$

that can be carefully measured with photodetector and lock-in amplifier locked to modulation frequency. Time dependence $P_r(t)$ is determined by the amplitude of spatial modulation a. In the case $a \ll \omega_0$ one can expand (3) in Taylor series. First-order approximation of the time-dependent part $P_r^{\sim}$ of the total reflected power [12]

$$P_r^{\sim}(x_p, y_p, t) \approx -a\sigma_a \left.\frac{\partial I(x,y)}{\partial x}\right|_{\substack{x=x_p \\ y=y_p}} \sin(2\pi ft) \quad (a \ll \omega_0) \tag{4}$$

is a simple sinusoidal function of time [Fig. 1(b)].

Taylor series expansion is not valid in a more general case of larger spatial modulation, when the time-dependent part $P_r^{\sim}(t)$ is a complicated periodic function that should be computed directly from (3) [Fig. 1(b)]. As lock-in measures the amplitude of the first harmonic, the output signal is determined by the corresponding coefficient b of the Fourier series expansion [14] of $P_r(t)$:

$$b(x_p, y_p) = 2f \int_{-1/(2f)}^{1/(2f)} I(x_p + a\sin(2\pi ft), y_p)\sin(2\pi ft)\, dt. \tag{5}$$

In the case of nonabsorbing particles the particle extinction is determined by the scattering of light. Scattering cross-section usually scales as a particle's volume squared [17], so that the detection of scattered light directly from small deeply subwavelength particles is typically hard or even impossible task for experiment. However, the situation can be greatly improved when detecting the interference of scattered and reflected light. Indeed, the interference signal is proportional to the electric field (i.e., square root of intensity) of the scattered light and scales linearly with the particle volume. For example, the 38-nm-diameter polystyrene spheres were detected in liquid flow by interferometric detection of forward scattered light [18]. It was shown [19,20] that this kind of interference can be analytically described under paraxial scalar approximation and Rayleigh approximation for scattered electric field.

When observed from the point with polar angle θ and azimuthal angle φ far from focus (the origin is assumed at the center of the beam waist, i.e., $x_c = y_c = 0$, focal plane at $z = 0$), the intensity contains an interference term δI caused by the particle at the point (x_p, y_p) of the focal plane. The optical system used for focusing laser beam converts this polar pattern to the corresponding distribution of intensity in its back focal plane. The specific pattern of this intensity modulation is antisymmetric with respect to the angle φ:

$$\delta I(x_p, y_p) \propto \frac{2\pi}{\lambda}(x_p\cos\varphi + y_p\sin\varphi)\exp\left(-\frac{x_p^2 + y_p^2}{\omega_0^2}\right). \tag{6}$$

Measuring the total power with a single photodetector as in the previous case is equivalent to integrating δI over φ in a full range from 0 to 2π and cannot detect this kind of interference signal. One can use a quadrant photodiode [19,20] or just block a half of the reflected beam at the back focal plane. In the latter case only half of the intensity pattern is integrated by the detector and the corresponding change in total power

$$\delta P(x_p, y_p) \propto \int_0^{\pi} \delta I(x_p, y_p)d\varphi \propto \frac{2\pi}{\lambda} 2y_p \exp\left(-\frac{x_p^2 + y_p^2}{\omega_0^2}\right). \tag{7}$$

Again, when the position of the particle in the focal plane is periodically changed with respect to the spot center, δP is modulated in time. However, due to the lack of axial symmetry of δP, the direction of the spot oscillation matters. For example, with the bottom half of the beam blocked, oscillation in x and y directions provides two possible unequivalent configurations ($\parallel$ and $\perp$, respectively) of scattering measurements:

$$\delta P_{\parallel}^{\sim}(x_p, y_p, t) \propto \frac{2\pi}{\lambda} 2y_p \exp\left(-\frac{(x_p + a\sin(2\pi ft))^2 + y_p^2}{\omega_0^2}\right),$$

$$\delta P_{\perp}^{\sim}(x_p, y_p, t) \propto \frac{2\pi}{\lambda} 2(y_p + a\sin(2\pi ft)) \times \exp\left(-\frac{x_p^2 + (y_p + a\sin(2\pi ft))^2}{\omega_0^2}\right). \tag{8}$$

The lock-in output is determined by the Fourier expansion coefficients

$$b_{\parallel,\perp}(x_p, y_p) = 2f \int_{-1/(2f)}^{1/(2f)} \delta P_{\parallel,\perp}^{\sim}(x_p, y_p, t)\sin(2\pi ft)\, dt, \tag{9}$$

The SMM "image" of the particle is determined by the spatial dependence of the expansion coefficients b and can be obtained by changing x_p, y_p, i.e., by step-by-step scanning of the sample.

III. IMPLEMENTATION OF SPATIAL MODULATION MICROSCOPY OF SILICON NANOPARTICLES

A. Samples

We study a commercially produced polished (001) p-Si wafer (doping level 1×10^{18} cm^{-3}) with nanoparticles at the surface. Cylindrical nanoparticles are patterned on the wafer surface using electron-beam lithography and subsequent plasma etching. We have two samples with different heights of nanocylinders above the silicon surface and different diameters: the first with nanocylinders of height $h = 20$ nm and diameters D ranging from 200 to 40 nm and the second with nanocylinders of height $h = 9$ nm and diameters ranging from 30 to 10 nm. In different patterned areas of both samples the distance between individual nanocylinders ranges from 1 to 10 μm. The size and shape of nanoparticles are controlled with scanning electron microscopy and atomic force microscopy. The roughness of the wafer surface without the nanocylinders is 0.2 nm root mean squared.

The studied nanocylinders are shown in the inset of Fig. 2(c). Owing to the indirect band structure, the contribution of the electron interband transitions to the complex dielectric constant of silicon varies by orders of magnitude. The fundamental absorption coefficient rises from approximately 10–100 cm^{-1} at wavelength around $\lambda \approx 1$ μm corresponding to the weak transitions to the indirect conduction band minimum, to approximately 10^5–10^6 cm^{-1} in the range $\lambda \approx 0.4$–0.35 μm when direct transitions in the center of the Brillouin zone become possible. At the same time, the real part of the dielectric constant changes only by a factor of three. Therefore, the same silicon nanocylinder can exhibit predominantly an absorbing or scattering particle behavior in different parts of visible-UV spectrum. Consequently, we can use the same samples to check the performance of both absorption-based and scattering-based SMM simply by tuning the wavelength to the desired range.

B. Experimental setup

Figure 2(a) shows our implementation of the SMM experimental setup. For easy spectral tuning, we use a femtosecond optical parametric oscillator (OPO) coupled to an Yb-doped solid-state ultrafast laser (150 fs, 80 MHz TOPOL + TEMA series, Avesta Project Ltd.) as a laser source for SMM experiments. Using additional custom optical frequency doubler (based on second harmonic generation in BBO crystal) we implemented SMM measurements in the spectral range from approximately 0.37 to approximately 1 μm.

The oscillation of the spot can be organized in a number of different ways. We use the deflection of the laser

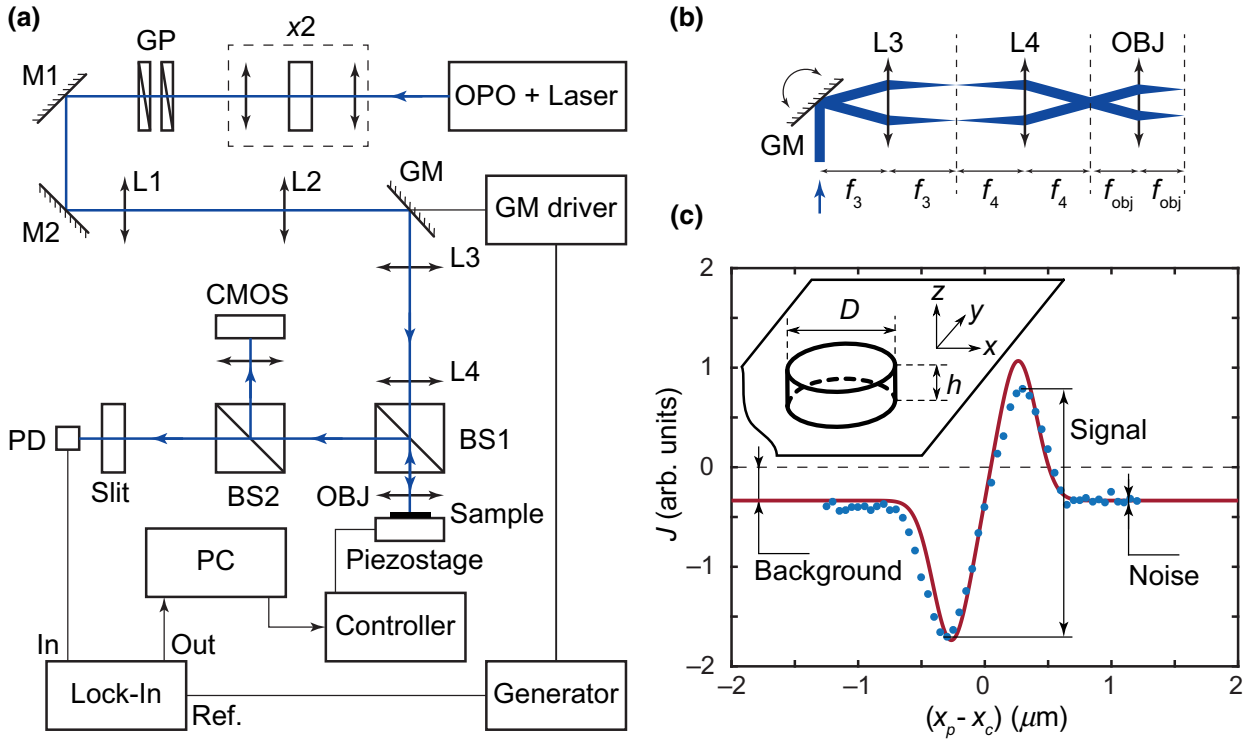

FIG. 2. (a) Schematics of the experimental setup. (b) Beam deflection principle (angles are highly exaggerated). (c) Photocurrent at deflection frequency when nanocylinder crosses the spot in the direction of deflection ($y_p = y_c$), measured data for $h = 20$ nm, $D = 40$ nm nanocylinder at $\lambda = 370$ nm (dots), and model (line). The inset shows the schematics of the samples studied in experiments.

beam by a galvo-mirror located at the focus of the $4f$ optical system coupled to the microscope objective. Laser light from the OPO output passes the optional frequency doubler and a pair of the Glan polarizers (GPs) for power control. We keep the average optical power below 1 mW. Two adjustment mirrors M1 and M2 direct the laser beam to the telescope lenses L1 and L2 and then to the galvo-mirror (GM). The GM is located in the focus of $4f$ system formed by lenses L3 and L4 that directs the collimated beam to the center of the entrance pupil of the infinity-corrected 100× objective lens (numerical aperture NA = 0.8) under different angles corresponding to the different rotations of the GM. An objective lens focuses the beam to a nearly diffraction-limited spot at the surface of the sample mounted at *XYZ* piezostage. The beam angle change at the back focal plane of the objective lens is converted into the focused spot position change at the sample surface. A schematic representation of the beam deflection is illustrated in Fig. 2(b). Lenses L3 and L4 are selected to achieve the desirable range of the amplitudes of spot movement under the working range of GM rotations. Lenses L1 and L2 are selected to fit the beam diameter to the objective lens aperture.

The reflected light is collected by the same objective lens. The cube beamsplitter BS1 is used to measure the average reflected beam power with a photodiode (PD). We also align a CMOS camera with the second beamsplitter BS2 and a tube lens for control of adjustment and sample surface navigation.

For interference detection we can block the half of the reflected beam in any place of the optical path between BS1 and PD. We use a slit before the PD for scattering measurements. The slit is adjusted in a such a way that one of the slit's blades blocks exactly one half of the beam. With deflection in the horizontal direction, blocking the top half of the beam corresponds to ∥ configuration, whereas blocking the left half of the beam corresponds to ⊥ configuration. Absorption measurements are taken with the slit fully open.

The function generator provides the control voltage for the GM in the form of a sinusoidal signal at frequency 1 kHz. The component J of the photodiode photocurrent at the deflection frequency is measured by SR830 lock-in amplifier. Custom software controls the piezostage movement for sample scanning and reading the lock-in output. During the scan, we change the position (x_p, y_p) of the nanocylinder with respect to the center of the spot (x_c, y_c). Figure 2(c) shows the dependence of J on the relative nanocylinder position $(x_p - x_c)$ along the direction of deflection (with $y_p = y_c$) together with the nanocylinder-related signal, background when nanocylinder is far from the spot, and noise. The recorded SMM image is a two-dimensional map of the photocurrent $J(x,y) \propto \sigma_a b(x,y)$ for absorption and $J(x,y) \propto \sqrt{\sigma_s} b_{\parallel,\perp}(x,y)$ for scattering measurements.

IV. IMAGING OF SILICON NANOCYLINDERS

Figure 3 shows registered experimental absorption SMM images of nanocylinders in the form of dependencies of the photocurrent J upon the relative positions of the nanocylinder with respect to the center of the spot.

Figure 3(a) shows the absorption-related signal of the smallest available nanocylinder with $h = 9$ nm and $D = 10$ nm, measured in UV, whereas Fig. 3(b) shows signal from the larger nanoparticle with $h = 20$ nm and $D = 40$ nm. Experimental images show a specific spatial profile similar to spatial derivative of the intensity distribution in the focal plane and agree well with a simulated image plotted in Fig. 3(c).

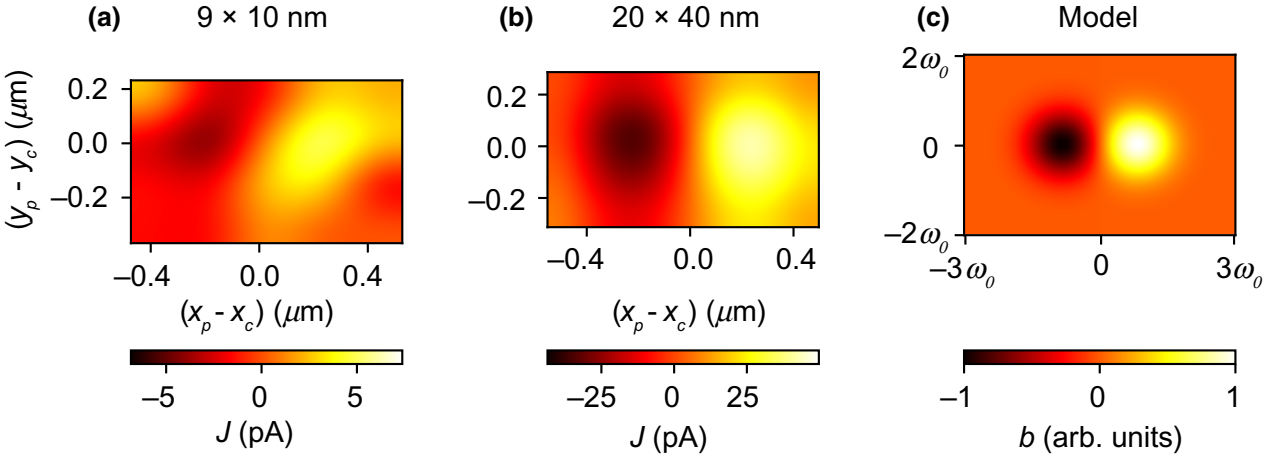

FIG. 3. Measured absorption SMM images of single nanocylinders with (a) $h = 9$ nm, $D = 10$ nm, $\lambda = 390$ nm and (b) $h = 20$ nm, $D = 40$ nm, $\lambda = 370$ nm. All images are measured with $a \approx \omega_0$, scan step 0.2 μm, and smoothed with bicubic interpolation. (c) Calculated SMM pattern $b(x_p, y_p)$ with $a = \omega_0$.

The absorption-based SMM is found to be a very sensitive tool for the detection of deeply subwavelength particles. The smallest available nanocylinder with $h = 9$ nm and $D = 10$ nm is detected with SNR $= 4.6$ with lock-in time constant 1 s (slope 12 dB/oct). Here the noise is a standard deviation of the signal from the flat surface without nanocylinders (background), that is mainly caused by the noise of the average laser intensity, which is measured to be $0.03\%/\sqrt{\text{Hz}}$ in the frequency range 0.2–2 kHz. It should be mentioned that the SMM background should be zero in the ideal case, because moving the spot along the flat surface provides no differential signal from the identical neighbor areas except the negligible contribution of the optical surface roughness scattering. However, in a real experimental setup there are a number of technical sources (small errors in adjustments, nonideal optics, and so on), that provide some small background signal that, nevertheless, can be offset by lock-in or subtracted in postprocessing.

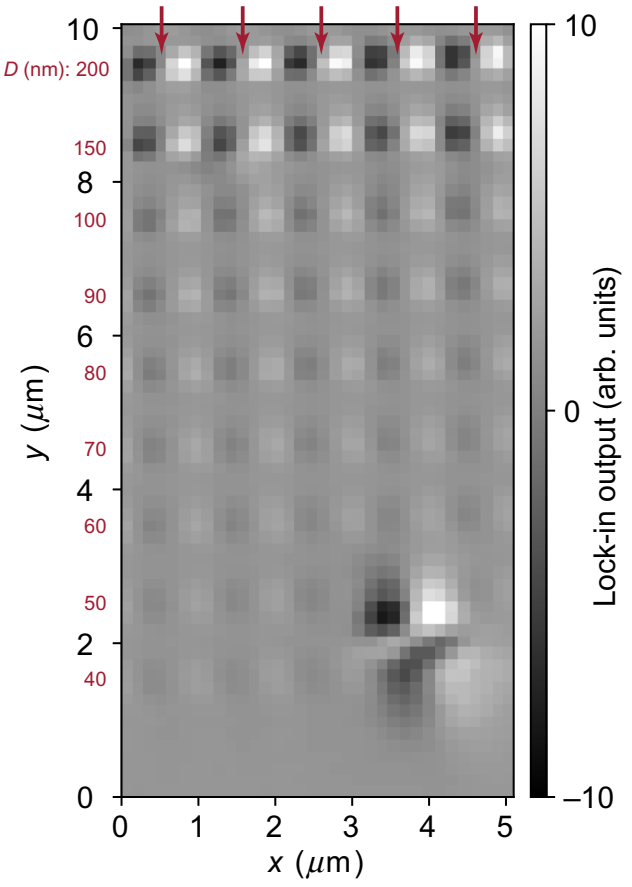

FIG. 4. Large-area scan of the sample with five columns of evenly patterned $h = 20$ nm nanocylinders with 1 μm pitch. Diameters of nanocylinders are shown in front of each row, $\lambda = 370$ nm. "Large" dust particle can be observed at the bottom right.

Figure 4 shows a raw image of a large area of the sample without any postprocessing. This area contains rows of nanocylinders with $h = 20$ nm and decreasing diameters from 200 to 40 nm evenly patterned in 1 μm pitch. In spite of the small spacing of the particles, all of them can be clearly distinguished together with an unknown larger dust particle located close to the 50 nm row. It should be noted, however, that the resolving power, that is, the distance between two particles where they are still distinguishable, is different in the x and y directions. In y direction, it is limited by a point spread function, whereas in the direction of deflection x, the differential response is wider than $2\omega_0$ even for small oscillation amplitudes a.

Figures 5(a) and 5(b) show images registered from a nanocylinder in visible red light related mostly to interference of the scattered and reflected light. Images are recorded in two configurations, $\parallel$ and $\perp$, with the top half and left half of the beam blocked and deflection of the spot in the horizontal direction. These two configurations are different in the sense of taking different parts of the interferometric perturbation of the intensity distribution and result in different symmetries of the SMM patterns. Scattering scans reveal this specific symmetry of spatial profiles expected from simulations shown in Figs. 5(c) and 5(d). The scattered signal is detected from all $h = 20$ nm nanocylinders, including the smallest with $D = 40$ nm in both configurations. However, $\perp$ configuration provides relatively high background signal related to time-varying clipping of the beam by a beam block.

We define a nanocylinder SMM signal S as a full peak-to-peak value of the corresponding spatial profile, so $S = \max[J(x,y)] - \min[J(x,y)]$. The total reflected power provides the DC photodiode output S_0 used for normalizing the SMM data. Figure 6 shows the scaling laws of the normalized nanocylinder SMM signals with its volume V. It is well known [17] that σ_a and σ_s of subwavelength nanoparticles scales as V and V^2, respectively. The experiment shows a close to linear dependence for the registered signals at visible range, confirming the interferometric nature of the effect when the measured signal is proportional to the $\sqrt{\sigma_s}$.

The dependence of the experimental absorption signal is also expected to be linear because it is directly proportional to σ_a. However, we find that the experimental dependence of absorption signal is sublinear. The best fit of data points from $h = 20$ nm nanocylinders with the power law is with the power exponent close to 0.7. Data points from $h = 9$ nm nanocylinders lay reasonably well on the line with the same scaling but shifted down (in log-log scale) by the factor corresponding to the difference in silicon absorption at the two wavelengths that the data are measured: the imaginary part of dielectric constant [21] $\text{Im}(\varepsilon(370\text{ nm})) = 26.95$ is about 3.9 times higher than $\text{Im}(\varepsilon(390\text{ nm})) = 6.93$.

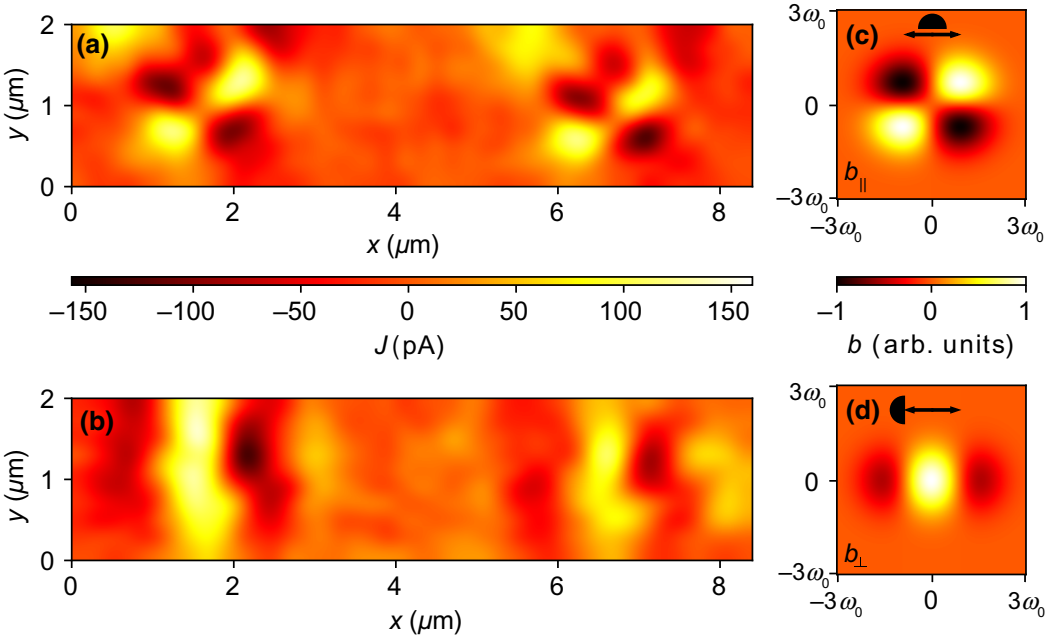

FIG. 5. Measured scattering SMM images of a pair of nanoparticles ($h = 20$ nm, $D = 80$ nm) at the distance 5 μm, $\lambda = 680$ nm: (a) the slit in the back focal plane blocks the top half of the beam; (b) the slit is rotated 90° so that it blocks the left half of the beam. Deflection is in horizontal direction. All images are measured with $a \approx \omega_0$, scan step 0.2 μm, and smoothed with bicubic interpolation. (c),(d) Calculated SMM patterns $b_{\parallel}(x_p, y_p)$ and $b_{\perp}(x_p, y_p)$, respectively, with $a = \omega_0$.

V. FEASIBILITY OF SPATIAL MODULATION MICROSCOPY FOR INDUSTRIAL APPLICATIONS

Our extension of the SMM technique paves the way toward pristine wafer diagnostics for the latest extreme ultraviolet (EUV) technology nodes. Here we outline the strategy for reduce the scanning time for the industry-standard 300 mm wafers. The time T for inspection of the whole wafer with the area A_w can be estimated as

$$T = \frac{A_w}{A_0}\tau_0, \tag{10}$$

where A_0 is the area of the spot and τ_0 is the measurement time at one spot position.

SMM requires a tightly focused beam because the signal is proportional to the derivative of the intensity profile. However, this requirement is in the direction of deflection only. We can increase A_0 from the currently used ≈ 0.5 μm diameter circular spot by using an elongated spot with long side perpendicular to the direction of deflection at the expense of precision of nanoparticle localization in the opposite direction. To check this assumption, and also to show that SMM can be used with any laser source, we perform test SMM measurements of a nanocylinder of $h = 20$ nm with inexpensive USB-powered 405 nm continuous-wave laser diode module and a cylindrical lens as a first lens of a $4f$ system (L3). This forms a spot in the form of a vertical line of approximately 0.5 μm width and several micrometers in height. With deflection in the horizontal direction, we obtain a reliably measurable signal when the $D = 40$ nm nanocylinder crosses the line at any vertical position during the sample scan. This, for a suitable spot (for example, 0.5×6 μm) the ratio $A_w/A_0 \approx 2.5 \times 10^{10}$.

SMM changes the approach from measuring extremely small scattered light power in scattering-based techniques to measuring a small modulation of moderate power of the reflected laser beam. In the first case, τ_0 is usually related to the exposure time needed to detect a few scattered photons and can be decreased only by an increase in the optical power of the laser source. In the second case, τ_0 is related to the number of the beam oscillations needed to achieve desired SNR and can be decreased with increasing the signal, decreasing the noise, and increasing the modulation frequency.

Moving to a shorter wavelength in the UV range is an obvious way to enhance signal with the benefit of λ^{-1} and λ^{-4} scaling of the σ_a and σ_s cross-sections [17]. The main noise source in our SMM measurements is the laser relative intensity noise (RIN). The well-known scheme for reducing this kind of noise is the balanced detection technique, which typically insures a two to three orders of rejection of the common-mode laser intensity noise. In order to increase the modulation frequency, the deflection of the spot can be implemented with fast acousto-optic deflector instead of a GM system [15].

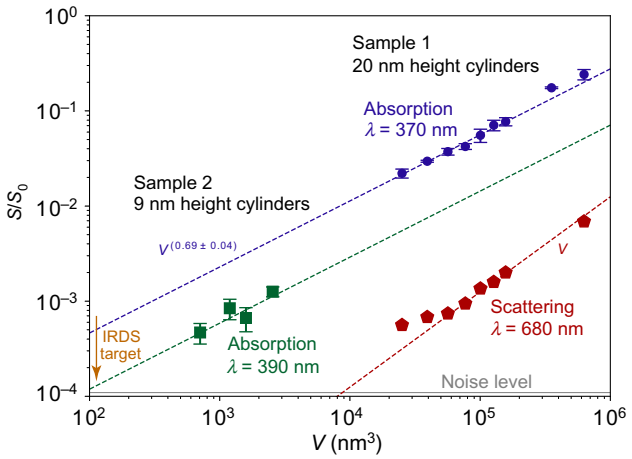

FIG. 6. Dependencies of the normalized absorption and scattering SMM signals on the nanocylinder volume. Absorption signals are measured at $\lambda = 370$ and 390 nm for two samples with different heights of nanocylinders, $h = 20$ nm (blue circles) and $h = 9$ nm (green squares), respectively. Error bars correspond to particle-to-particle dispersion. Scattering signals are measured at $\lambda = 680$ nm for one sample with $h = 20$ nm nanocylinders in $\parallel$ configuration. The red dashed line shows the linear fit of scattering experimental signal for $h = 20$ nm nanocylinders. The blue dashed line is the V^p law fit with $p = 0.69 \pm 0.04$ for absorption signal at $\lambda = 370$ nm, whereas the green line is shifted to the ratio of imaginary parts of silicon dielectric constant $\mathrm{Im}(\varepsilon(370\ \mathrm{nm}))/\mathrm{Im}(\varepsilon(390\ \mathrm{nm})) \approx 3.9$. The arrow shows the volume of a 6 nm spherical particle specified as a critical size in IRDS [3].

Currently commercially available acousto-optic deflectors have sweep bandwidth of tens of megahertz and operating wavelength up to 266 nm. Using a 266 nm laser source increases the σ_a (σ_s) by a factor of approximately 1.4 (3.8). Increasing the modulation frequency from 1 kHz to 10 MHz and reducing the intensity noise by two orders of magnitude, we can decrease the measurement time τ_0 at one spot position from current 1 s to about 10 μs keeping the same SNR. This gives the scan time for the whole 300 mm wafer $T = 2.5 \times 10^5$ s (about 69.5 h), which can be further reduced to a "comfortable" less-than-one-day level with parallelization of the scan into several independent measurement channels.

Special attention should be paid to noise sources during increasing the frequency of oscillations to avoid the degradation of SNR. The typical spectrum of RIN contains a sharp peak at the resonant relaxation oscillation frequency (see, for example, [22]) in tens-to-hundreds of kilohertz range for solid-state lasers. For higher frequencies, RIN usually rapidly decreases down to shot noise level, so the high-frequency modulation reduces the RIN contribution. Typical levels of electronic noise of balanced photodetectors based on common transimpedance amplifier schematics are below the shot-noise level in all working bandwidth up to tens of megahertz [23]. Fast acousto-optic deflection can introduce new sources of noise. Small changes in diffraction efficiency associated with the deflection can be compensated for with corresponding small-amplitude modulation of the driving power to minimize the intensity modulation of the deflected laser beam. Noise related to fluctuations of the diffraction efficiency can be suppressed with optimization of the driving power [24].

One of the advantages of SMM for scattering particles we would like to emphasize is the slow decline of the signal with the decrease of both particle size and particle refractive index. Typical nanoparticles of interest, such as polystyrene or silicon dioxide nanobeads, have material refractive indices two to three times less than silicon studied in this work. However, SMM gives the edge over traditional methods of direct measurements of scattered light intensity with both background suppression and square-root signal scaling with the scattering cross-section due to the differential interferometric principle of the technique.

SMM is based on a relatively simple optical layout and can use existing laser scanning microscopy platforms, providing a useful extension for the detection of sub-10-nm particles. An interesting possibility is a combination of this differential technique with nonlinear optical microscopy in cases when the nonlinear nanoparticle response itself is the subject of the study. SMM provides an easy separation of the nanoparticle response from the background response of the substrate and can be used, for example, for the extraction of the weak enhancement of the harmonic generation [11] or nonlinear photoluminescence [10] by the surface particles. However, the application in silicon surface inspection is limited by the low overall efficiency of Si nonlinear response.

VI. CONCLUSION

We find a potential solution for wafer quality control for EUV technology nodes. We develop a SMM technique for far-field optical detection of deeply subwavelength absorbing and scattering nanoparticles. We demonstrate the linear dependence of the scattering SMM signal (visible range) on the nanoparticle's volume, as expected due to interferometric nature of the effect. We find the sublinear dependence of the absorption SMM signal (UV range) on the nanoparticle's volume ($\sim V^{0.7}$). Using the developed technique we demonstrate experimentally the optical detection of a 10-nm silicon nanoparticle on the silicon surface. SMM can be used as an additional channel of optical inspection in modern semiconductor inspection tools.

ACKNOWLEDGMENTS

We thank the MRDC team (Core Technology R&D Team, Mechatronics R&D Center, Samsung Electronics,

Hwaseong-si, Korea) for the provided samples and fruitful discussion.

[1] N. G. Orji, M. Badaroglu, B. M. Barnes, C. Beitia, B. D. Bunday, U. Celano, R. J. Kline, M. Neisser, Y. Obeng, and A. E. Vladar, Metrology for the next generation of semiconductor devices, Nat. Electron. **1**, 532 (2018).

[2] A. Diebold, *Handbook of Silicon Semiconductor Metrology* (CRC Press, New York, 2001).

[3] *International Roadmap for Devices and Systems* (IEEE, Piscataway, 2020), https://irds.ieee.org/images/files/pdf/2020/2020IRDS_MET.pdf.

[4] S. Cho, J. Lee, H. Kim, S. Lee, A. Ohkubo, J. Lee, T. Kim, S. Bae, and W. Joo, Super-contrast-enhanced dark-field imaging of nano objects through null ellipsometry, Opt. Lett. **43**, 5701 (2018).

[5] S. Berciaud, D. Lasne, G. A. Blab, L. Cognet, and B. Lounis, Photothermal heterodyne imaging of individual metallic nanoparticles: Theory versus experiment, Phys. Rev. B **73**, 045424 (2006).

[6] Y. Wang, C.-Y. Lin, A. Nikolaenko, V. Raghunathan, and E. O. Potma, Four-wave mixing microscopy of nanostructures, Adv. Opt. Photonics **3**, 1 (2011).

[7] F. Masia, W. Langbein, and P. Borri, Measurement of the dynamics of plasmons inside individual gold nanoparticles using a femtosecond phase-resolved microscope, Phys. Rev. B **85**, 235403 (2012).

[8] X. Hong, E. M. P. H. van Dijk, S. R. Hall, J. B. Götte, N. F. van Hulst, and H. Gersen, Background-free detection of single 5 nm nanoparticles through interferometric cross-polarization microscopy, Nano Lett. **11**, 541 (2011).

[9] B. T. Miles, E. C. Robinson, E. M. H. P. van Dijk, I. D. Lindsay, N. F. van Hulst, and H. Gersen, Sensitivity of interferometric cross-polarization microscopy for nanoparticle detection in the near-infrared, ACS Photonics **2**, 1705 (2015).

[10] B. I. Afinogenov, A. S. Medvedev, I. M. Antropov, N. R. Filatov, A. N. Sofronov, E. Jeang, S. Bae, T. Kim, I. Kim, A. Ohkubo, S. Lee, S. Lee, W. Joo, M. Seo, A. S. Shorokhov, V. O. Bessonov, and M. V. Ryabko, in *Nanoengineering: Fabrication, Properties, Optics, Thin Films, and Devices XVII*, edited by B. Panchapakesan, A.-J. Attias, and W. Park, International Society for Optics and Photonics, Vol. 11467 (SPIE, Bellingham, WA, 2020), p. 101.

[11] E. Jeang, B. Afinogenov, S. Bae, T. Kim, I. Kim, K. Han, A. Ohkubo, S. Lee, M. Seo, S. Lee, W. Joo, H. Yoo, A. Medvedev, A. Shorokhov, A. Sofronov, M. Riabko, V. Bessonov, and I. Antropov, in *Nonlinear Optics and its Applications 2020*, edited by N. G. R. Broderick, J. M. Dudley, and A. C. Peacock, International Society for Optics and Photonics, Vol. 11358 (SPIE, Bellingham, WA, 2020), p. 1.

[12] A. Arbouet, D. Christofilos, N. Del Fatti, F. Vallée, J. R. Huntzinger, L. Arnaud, P. Billaud, and M. Broyer, Direct Measurement of the Single-Metal-Cluster Optical Absorption, Phys. Rev. Lett. **93**, 127401 (2004).

[13] O. L. Muskens, P. Billaud, M. Broyer, N. Del Fatti, and F. Vallée, Optical extinction spectrum of a single metal nanoparticle: Quantitative characterization of a particle and of its local environment, Phys. Rev. B **78**, 205410 (2008).

[14] M. P. McDonald, F. Vietmeyer, D. Aleksiuk, and M. Kuno, Supercontinuum spatial modulation spectroscopy: Detection and noise limitations, Rev. Sci. Instrum. **84**, 113104 (2013).

[15] M. S. Devadas, Z. Li, T. A. Major, S. S. Lo, N. Havard, K. Yu, P. Johns, and G. V. Hartland, Detection of single gold nanoparticles using spatial modulation spectroscopy implemented with a galvo-scanning mirror system, Appl. Opt. **52**, 7806 (2013).

[16] T. Devkota, M. S. Devadas, A. Brown, J. Talghader, and G. V. Hartland, Spatial modulation spectroscopy imaging of nano-objects of different sizes and shapes, Appl. Opt. **55**, 796 (2016).

[17] C. Bohren and D. Huffman, *Absorption and Scattering of Light by Small Particles*, Wiley Science Series (Wiley-VCH, Weinheim, 2008).

[18] J. S. Batchelder and M. A. Taubenblatt, Interferometric detection of forward scattered light from small particles, Appl. Phys. Lett. **55**, 215 (1989).

[19] F. Gittes and C. F. Schmidt, Interference model for back-focal-plane displacement detection in optical tweezers, Opt. Lett. **23**, 7 (1998).

[20] M. W. Allersma, F. Gittes, M. J. deCastro, R. J. Stewart, and C. F. Schmidt, Two-dimensional tracking of ncd motility by back focal plane interferometry, Biophys. J. **74**, 1074 (1998).

[21] D. E. Aspnes and A. A. Studna, Dielectric functions and optical parameters of Si, Ge, GaP, GaAs, GaSb, InP, InAs, and InSb from 1.5 to 6.0 eV, Phys. Rev. B **27**, 985 (1983).

[22] C. C. Harb, T. C. Ralph, E. H. Huntington, I. Freitag, D. E. McClelland, and H.-A. Bachor, Intensity-noise properties of injection-locked lasers, Phys. Rev. A **54**, 4370 (1996).

[23] A. V. Masalov, A. Kuzhamuratov, and A. I. Lvovsky, Noise spectra in balanced optical detectors based on transimpedance amplifiers, Rev. Sci. Instrum. **88**, 113109 (2017).

[24] F. Liu, L. Gu, S. Xie, X. He, D. Yi, M. Zhang, and Q. Tao, Acousto-optic modulation induced noises on heterodyne-interrogated interferometric fiber-optic sensors, J. Lightwave Technol. **36**, 3465 (2018).